Chemical Engineering Journal 308 (2017) 184–192

Contents lists available at ScienceDirect

Chemical Engineering Journal

journal homepage: www.elsevier.com/locate/cej

Synthesis and remarkable capacitive performance of reduced graphene oxide/silver/nickel-cobalt sulfide ternary nanocomposites

Xiaoqing Cai [a], Xiaoping Shen [a,*], Zhenyuan Ji [a], Xuexi Sheng [a], Lirong Kong [a], Aihua Yuan [b]

[a] School of Chemistry and Chemical Engineering, Jiangsu University, Zhenjiang 212013, PR China
[b] School of Environmental and Chemical Engineering, Jiangsu University of Science and Technology, Zhenjiang 212003, PR China

HIGHLIGHTS

- RGO/Ag/$NiCo_2S_4$ nanocomposites were synthesized through an efficient two-step solution route.
- Ag and $NiCo_2S_4$ nanoparticles were well combined with RGO sheets.
- RGO/Ag/$NiCo_2S_4$ nanocomposites have remarkable capacitive performances.
- Possible mechanism for the enhanced capacitive performance was proposed.

ARTICLE INFO

Article history:
Received 19 June 2016
Received in revised form 23 August 2016
Accepted 12 September 2016
Available online 12 September 2016

Keywords:
Reduced graphene oxide
Ag
$NiCo_2S_4$
Nanocomposite
Supercapacitor

ABSTRACT

Highly uniform ternary nanocomposites of reduced graphene oxide/silver/nickel-cobalt sulfide (RGO/Ag/$NiCo_2S_4$) are successfully prepared by an efficient two-step solution route. In the nanocomposites, Ag and $NiCo_2S_4$ nanoparticles with sizes of several nanometers are homogeneously anchored on the surface of RGO sheets. The RGO/Ag/$NiCo_2S_4$ nanocomposites are used as electrode materials for supercapacitors and their capacitive performance are investigated. It is found that their capacitive performances are remarkably affected by the Ag content. The RGO/Ag/$NiCo_2S_4$ nanocomposites exhibit excellent specific capacitance as high as 2438 F g^{-1} at the current density of 2.0 A g^{-1}, good rate capability with a specific capacitance of 1410 F g^{-1} at the high current density of 20 A g^{-1}, and high cycling stability with 85.4% capacitance retention after 2000 charge-discharge cycles at the current density of 10 A g^{-1}. The enhanced capacitive performance can be attributed to the synergistic effect among $NiCo_2S_4$, Ag and RGO, in which RGO sheets serve as an ideal support matrix and Ag nanoparticles act as conductive channels. The remarkable capacitive performance of RGO/Ag/$NiCo_2S_4$ makes it a promising candidate for supercapacitor electrode materials.

1. Introduction

The global environmental pollution and the depletion of fossil fuels have stimulated the endeavors to develop not only new clean energies but also highly effective energy conversion/storage systems. Supercapacitors, a type of energy storage device, have been attracting great attention due to their significant advantages beyond rechargeable batteries in terms of power density and cycling life. The great requirement for instantaneous and uninterruptable power makes them promising application in heavy transport and electric vehicles [1–3]. However, the energy density of supercapacitors is relatively lower than that of rechargeable batteries. Therefore, the improvement of the energy density without sacrificing the power density and the cycle life is a major challenge for current supercapacitor technology, which needs to be further exploited [4–6].

Generally, supercapacitors can be classified into double layer capacitors and pseudocapacitors based on their different charge storage mechanisms [7]. Pseudocapacitors involve electrochemical faradic reactions between electrode materials and the electrolyte, thus contributing to a higher energy density than that of double layer capacitors [8]. Therefore, the development of electrode materials with high performance for pseudocapacitors becomes a research hotspot. Recently, transition metal sulfides have been studied as a new type of pseudocapacitor electrode materials [9–11]. Particularly, $NiCo_2S_4$ has aroused intense interest due to its rich redox characteristic, excellent electrochemical activity, low cost and relatively higher electronic conductivity than that of the corresponding monometallic Ni or Co sulfides [12], and some

* Corresponding author.
E-mail address: xiaopingshen@163.com (X. Shen).

http://dx.doi.org/10.1016/j.cej.2016.09.059
1385-8947/

works about $NiCo_2S_4$-based electrode materials for pseudocapacitors have been reported in recent years [13–18]. For instance, Pu et al. reported $NiCo_2S_4$ hollow hexagonal nanoplates with a specific capacitance of 437.0 F g^{-1} at a charge-discharge current density of 1.0 A g^{-1} [13]. Yu et al. reported $Ni_xCo_{3-x}S_4$ hollow nanoprisms with a specific capacitance of 895.2 F g^{-1} at 1.0 A g^{-1} [15]. Wan et al. reported $NiCo_2S_4$ porous nanotubes with a specific capacitance of 933.0 F g^{-1} at 1.0 A g^{-1} [18]. However, the electrochemical performance of these $NiCo_2S_4$ nanostructures is still limited by its poor electrical conductivity and the structural degradation, which deteriorate the specific capacitance, rate capability and cyclic stability of the $NiCo_2S_4$ electrodes. Thus, further efforts are needed to develop new $NiCo_2S_4$-based electrode materials with improved electrochemical performance.

Recently, hybridizing active psedocapacitive components with carbonaceous materials has been proved to be an effective approach to improve electron transport rate, electrolyte contact area and structural stability, all of which are beneficial for electrochemical performance [19,20]. In particular, graphene with excellent electronic conductivity, high surface area (theoretical value: 2630 m^2/g) and good mechanical performance has been considered as a promising type of carbonaceous supporting materials [21,22]. Compared with zero-dimensional carbon nanoparticles and one-dimensional carbon nanotubes, graphene with two-dimensional structure is easier and more flexible to integrate with other components. Graphene/metal oxides or sulfides composite electrodes have been widely investigated recently [23–25]. It is found that the introduction of graphene as a flexible matrix could effectively improve the electrochemical performance of active components. In addition, recent research have demonstrated that the capacitive property of graphene-based materials can be further improved by attaching noble metal nanoparticles, which not only act as the spacer to prevent the graphene sheets from aggregation, but also create additional electron transfer pathways [26,27]. Therefore, combination of active components with graphene as well as noble metal nanoparticles could be a promising route to achieve enhanced electrochemical performance. In this work, we demonstrated an efficient two-step solution route for the preparation of reduced graphene oxide (RGO)/Ag/$NiCo_2S_4$ ternary nanocomposites, in which Ag and $NiCo_2S_4$ nanoparticles with sizes of several nanometers are homogeneously dispersed on the surface of RGO sheets. The RGO/Ag/$NiCo_2S_4$ nanocomposites as electrode materials exhibit extraordinary specific capacitance, good rate capability and high cycling stability, indicating a promising application in supercapacitor electrodes.

2. Experimental

2.1. Materials

Natural flake graphite with a particle size of 150 μm (99.9% purity) was purchased from Qingdao Guyu Graphite Co., Ltd. Anisole and oleylamine (C_{18}: 80–90%) (OLA) were purchased from Aladdin Industrial Corporation (Shanghai, China). The other chemical reagents were purchased from Sinopharm Chemical Reagent Co. China. All of the reagents employed in this research are of A. R. grade and were used without further purification. Graphite oxide was synthesized from natural flake graphite using a modified Hummers method [28,29].

2.2. Synthesis of $NiCo_2S_4$ nanoparticles

In this experiment, $NiCo_2S_4$ nanoparticles were synthesized according to the following procedures: 0.2 mmol of $Ni(Ac)_2{\cdot}H_2O$, 0.4 mmol of $Co(Ac)_2{\cdot}H_2O$, 0.8 mmol of sulfur powder and 3.5 mL of oleylamine were dissolved in 20 mL anisole by magnetic stirring. Then the mixed solution was transferred into a 40 mL Teflon-lined stainless steel autoclave, and maintained at 180 °C for 24 h. After the reaction system was cooled to room temperature, the sediment was collected by centrifugation and washed several times with cyclohexane and ethanol. Finally, the as-obtained black product was dispersed into 20 mL of DI water by ultrasonication for further utilization.

2.3. Synthesis of RGO/Ag/$NiCo_2S_4$ nanocomposites

RGO/Ag nanocomposites were firstly prepared by a refluxing method. Typically, 10 mg of graphite oxide was dispersed in 20 mL of DI water by ultrasonication. Subsequently, 3 mL of freshly prepared $AgNO_3$ aqueous solution (1 mg/mL) was added into the above suspension. After vigorous stirring for 2 h, 5 mL of NaOH solution (0.5 M) was introduced gradually under magnetic stirring. Then the resultant suspension was transferred into a 100 mL round-bottomed flask and refluxed at 95 °C for 1 h. The precipitates (RGO/Ag nanocomposites) were collected and washed with DI water and ethanol, respectively. Subsequently, the RGO/Ag nanocomposites were dispersed in 20 mL of DI water to form a suspension, into which the pre-prepared $NiCo_2S_4$ aqueous dispersion was introduced, and followed by vigorous stirring for 20 h. The black product (RGO/Ag/$NiCo_2S_4$ nanocomposites) was separated by centrifugation and dried under vacuum at 45 °C. For comparison, RGO/Ag/$NiCo_2S_4$ nanocomposites with different Ag contents were synthesized by changing the dosage of $AgNO_3$ in the synthesis. The obtained products were designated as RGO/Ag/$NiCo_2S_4$-1, RGO/Ag/$NiCo_2S_4$-2, RGO/Ag/$NiCo_2S_4$-3 and RGO/Ag/$NiCo_2S_4$-4 for the feeding amount of 1, 2, 3 and 4 mL of $AgNO_3$ aqueous solution, respectively. In addition, RGO/$NiCo_2S_4$ was also synthesized in the same way as the RGO/Ag/$NiCo_2S_4$ nanocomposites in the absence of $AgNO_3$.

2.4. Instruments and characterization

The phase structures of the products were characterized by powder X-ray diffraction (XRD, Bruker D8 Advance) equipped with Cu Kα radiation source (λ = 1.5406 Å) at a scanning rate of 4° min^{-1}. The compositions of the products were determined by energy-dispersive X-ray spectrometry (EDS). The element contents were determined by atomic absorption spectrometer (AAS, TAS-986). Raman spectra were performed on a JYHR800 Raman spectrometer using a 532 nm laser source. The morphology and microstructure analysis of the products were investigated by a JEOL-2100 transmission electron microscopy (TEM) with an acceleration voltage of 200 kV. The Brunauer-Emmett-Teller surface areas have been tested by a surface area and porosity analyzer (NDVA-2000e).

2.5. Electrochemical measurements

For the fabrication of working electrodes for supercapacitor, the nickel foams (surface area: 1.0 × 2.0 cm^2, thickness: 1.0 mm, pore density: 110 PPI) were firstly washed with ethanol, acetone, and DI water to remove contaminants on the surface. Active materials (RGO/Ag/$NiCo_2S_4$ composites or RGO/$NiCo_2S_4$ composite) were mixed with conductive agent (acetylene black) and poly(vinylidene fluoride) (PVDF) binder in a weight ratio of 8:1:1. *N*-Methyl-2-pyrrolidone as solvent was then introduced into the mixture. With continuous stirring for 24 h to form milk-like slurry, the slurry was coated on the surface of the cleaned nickel foam and then dried at 45 °C in a vacuum oven. Finally, the electrodes loaded with active material were pressed at 10 MPa.

The electrochemical measurements were carried out at room temperature in a three-electrode system on the CHI 760D electrochemical work-station (Shanghai, Chenhua Co.) with 3.0 M KOH solution as electrolyte. The as-prepared RGO/Ag/$NiCo_2S_4$ nanocomposite electrode, Pt foil and saturated calomel electrode (SCE) were used as the working electrode, counter electrode and reference electrode, respectively. The electrochemical properties of the obtained products were evaluated by cyclic voltammetry (CV), galvanostatic charge-discharge (GCD) and electrochemical impedance spectroscopy (EIS).

3. Results and discussion

3.1. Structural and morphological characterization

In this research, we develop an effective two-step solution route for synthesis of RGO/Ag/$NiCo_2S_4$ ternary nanocomposites, and the synthetic process is illustrated in Scheme 1. RGO/Ag nanocomposites were firstly synthesized by in-situ growth and co-reduction process. It is known that graphite oxide (GO) contains carboxyl and phenolic hydroxyl groups on the edges and surfaces. When dispersed in DI water, GO sheets are highly negatively charged due to the ionization of the oxygen-containing functional groups. Silver ions with positive charges were easily absorbed on the surface of GO sheets by the electrostatic interaction. When NaOH solution was added, the phenolic hydroxyl groups on the surface of GO sheets were deprotonated to form phenolate anions, which transfer electrons to Ag^+ to form metallic Ag nanoparticles by electrophilic aromatic substitution [27]. At the same time, GO was converted into RGO under the strong alkaline conditions [30,31]. Therefore, NaOH plays a dual role, which not only accelerates the reduction of Ag^+ by GO, but also induces the reduction of GO into RGO. Furthermore, when $NiCo_2S_4$ nanoparticles were introduced into the RGO/Ag suspension, they were anchored on the surface of RGO/Ag by a self-assembly process. As a result, RGO/Ag/$NiCo_2S_4$ ternary nanocomposites were obtained successfully.

3.2. Structural and morphological characterization

Crystal phases of the synthesized products were firstly determined by XRD. Fig. 1a shows the XRD patterns of graphite oxide, RGO/Ag, RGO/$NiCo_2S_4$ and RGO/Ag/$NiCo_2S_4$-3 nanocomposite. For graphite oxide, a strong diffraction peak centered at $2\theta = 10.8°$ is corresponding to the characteristic peak (0 0 1) of graphite oxide. In the XRD pattern of RGO/Ag nanocomposite, the (0 0 1) peak of graphite oxide disappears, indicating that graphite oxide has been well flaked to GO and/or subsequently reduced into RGO. Moreover, two characteristic peaks at $2\theta = 38.1°$ and 44.2° occur, which are well indexed to (1 1 1) and (2 0 0) planes of the cubic phase Ag (JCPDS No. 65-2871), respectively. This result confirms that Ag^+ have been successfully reduced to metallic Ag. Two weak peaks at about 11° and 30° in the XRD pattern of RGO/Ag originate from the SiO_2 substrate used for XRD measurement. For RGO/$NiCo_2S_4$ composite, the spectrum shows the diffraction peaks located at 26.0°, 31.5°, 38.3°, 50.4° and 54.8°, which can be well indexed to the (2 2 0), (3 1 1), (4 0 0), (5 1 1) and (4 4 0) reflections of the cubic phase $NiCo_2S_4$ (JCPDS No. 20-0782). Similarly, the (0 0 1) peak of graphite oxide was not detected due to its exfoliation and/or reduction. The XRD pattern of RGO/Ag/$NiCo_2S_4$ nanocomposite consists of $NiCo_2S_4$ and Ag diffraction peaks with the characteristic peak (1 1 1) of Ag overlapping the diffraction peak (4 0 0) of $NiCo_2S_4$, indicating successful synthesis of the RGO/Ag/$NiCo_2S_4$ nanocomposite. In addition, the broad and weak peak at about 21° in the XRD patterns of RGO/$NiCo_2S_4$ and RGO/Ag/$NiCo_2S_4$ can be attributed to the (0 0 2) peak of RGO, which is typical of turbostratic graphitic structure. The EDS of RGO/Ag/$NiCo_2S_4$-3 nanocomposite is shown in Fig. S1. The elements of C, O, Co, Ni, S and Ag are detected, which provide further evidence for the formation of RGO/Ag/$NiCo_2S_4$ ternary nanocomposite. The contents of Ag, Ni and Co in the samples were determined by atomic absorption spectrometer (AAS), the detailed parameters are shown in the Table 1. It can be observed that the contents of Ni and Co decrease gradually with the increase of Ag content, suggesting that the increased Ag content will lower the content of the active component.

Raman spectroscopy is widely used to characterize the disorder and defect structure of graphene-based materials [32]. Raman spectra of RGO/Ag/$NiCo_2S_4$-3 nanocomposite, RGO/Ag composite and graphite oxide were shown in Fig. 1b. All of the spectra display two prominent peaks, corresponding to the well-documented D and G bands, respectively. It is known that D band originates from a breathing mode of a κ-point phonon of A_{1g} symmetry related to

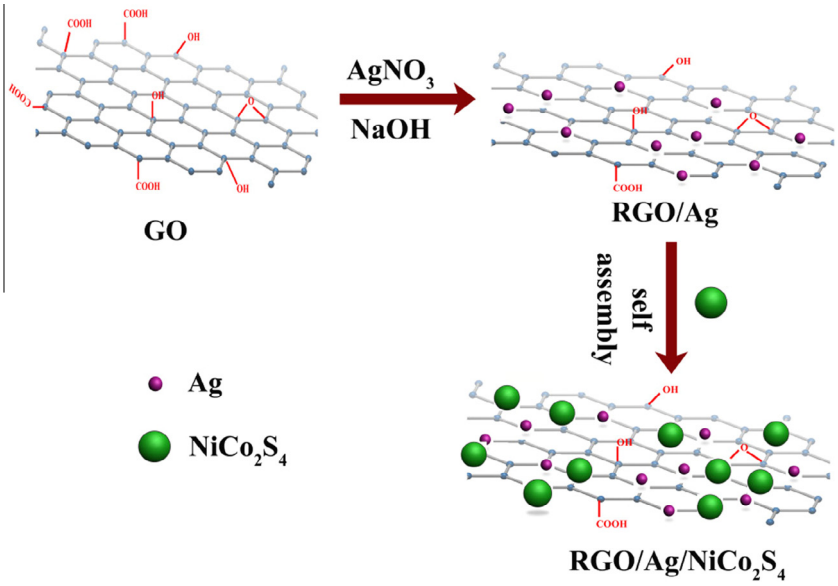

Scheme 1. Illustration of the formation process of RGO/Ag/$NiCo_2S_4$ nanocomposites.

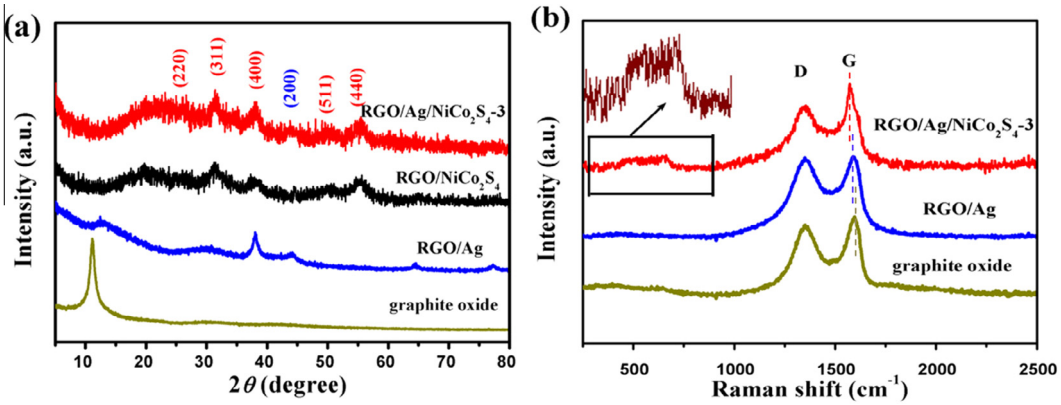

Fig. 1. (a) XRD patterns of graphite oxide, RGO/Ag, RGO/$NiCo_2S_4$ and RGO/Ag/$NiCo_2S_4$-3 nanocomposite; (b) Raman spectra of graphite oxide, RGO/Ag and RGO/Ag/$NiCo_2S_4$-3 nanocomposite. The inset in (b) is a local magnified view of Raman spectrum of RGO/Ag/$NiCo_2S_4$-3 nanocomposite.

Table 1
The contents of Ag, Ni and Co in the samples determined by AAS.

Element contents (wt%)	Samples				
	RGO/$NiCo_2S_4$	RGO/Ag/$NiCo_2S_4$-1	RGO/Ag/$NiCo_2S_4$-2	RGO/Ag/$NiCo_2S_4$-3	RGO/Ag/$NiCo_2S_4$-4
Ag	0	1.3%	2.4%	3.0%	4.3%
Ni	16.4%	15.4%	15.1%	14.8%	14.5%
Co	33.0%	32.7%	31.5%	30.4%	29.4%

local defects and disorder, while G band is usually assigned to the E_{2g} symmetric vibrational mode of graphene sp^2 C atoms [33]. It can be observed that the G band moves from 1598 cm^{-1} for graphite oxide to 1591 cm^{-1} for RGO/Ag and 1584 cm^{-1} for RGO/Ag/$NiCo_2S_4$-3 nanocomposite, respectively. The shift of G band towards the value of pristine graphite (1581 cm^{-1}) further confirms the reduction of graphite oxide [37]. The intensity ratio of D to G band (I_D/I_G) is usually used to evaluate the degree of graphitization and defects [34,35]. By a Gaussian fitting method, the I_D/I_G values are calculated to be 1.5, 1.9 and 2.0 for graphite oxide, RGO/Ag and RGO/Ag/$NiCo_2S_4$-3 nanocomposite, respectively. The increased I_D/I_G values for RGO/Ag and RGO/Ag/$NiCo_2S_4$-3 nanocomposite compared to graphite oxide indicate that GO has been well deoxygenated and reduced to RGO [36]. Furthermore, besides the Raman peaks from RGO, two weak peaks at 515.3 cm^{-1} and 664.2 cm^{-1} are also observed in RGO/Ag/$NiCo_2S_4$-3 nanocomposite. The local magnified view is presented in the inset of Fig. 1b for clarity. The two peaks correspond to the F_{2g} and A_{1g} models of $NiCo_2S_4$, respectively [38].

The detailed morphology, size and microstructure of the as-prepared samples were examined by TEM and high resolution TEM (HRTEM). TEM images of RGO/Ag nanocomposite are presented in Fig. 2, from which Ag nanoparticles anchored on RGO sheets with highly uniform distribution can be clearly seen. Due to the low loading amount of Ag, RGO sheets are only partly covered by Ag nanoparticles. Fig. 3 displays the representative TEM (HRTEM) images of the RGO/Ag/$NiCo_2S_4$-3 nanocomposite. Due to the high content of $NiCo_2S_4$, the whole surface of RGO/Ag sheets is densely covered by $NiCo_2S_4$ nanoparticles (Fig. 3a). No free nanoparticles are detected outside of the RGO sheets, suggesting that the nanoparticles are well combined with RGO. Fig. 3b and c show TEM images with higher magnification, which reveal the distribution detail of Ag and $NiCo_2S_4$ nanoparticles on RGO. As shown in Fig. 3b, RGO edges with a wrinkled silk wave-like morphology that graphene intrinsically owns can be discerned (as marked with white arrows). Due to Ag nanoparticles with small size anchoring on the surface of RGO sheets firstly, $NiCo_2S_4$ nanoparticles occupy the sites that Ag nanoparticles have

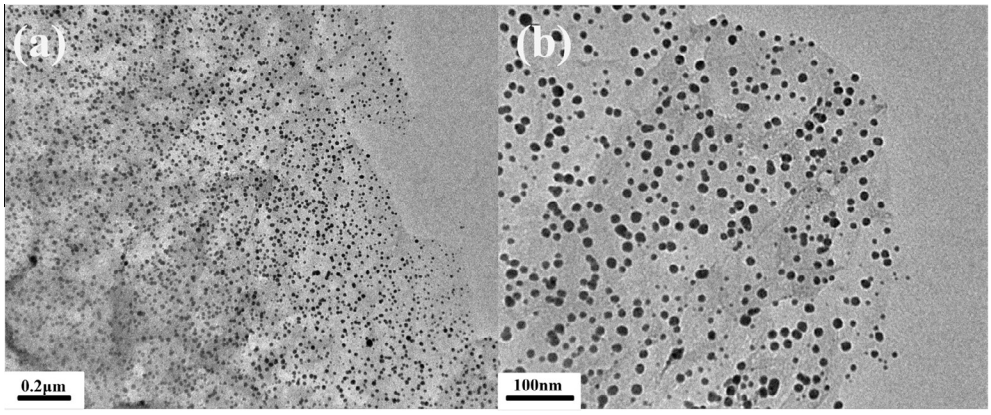

Fig. 2. TEM images of RGO/Ag nanocomposite.

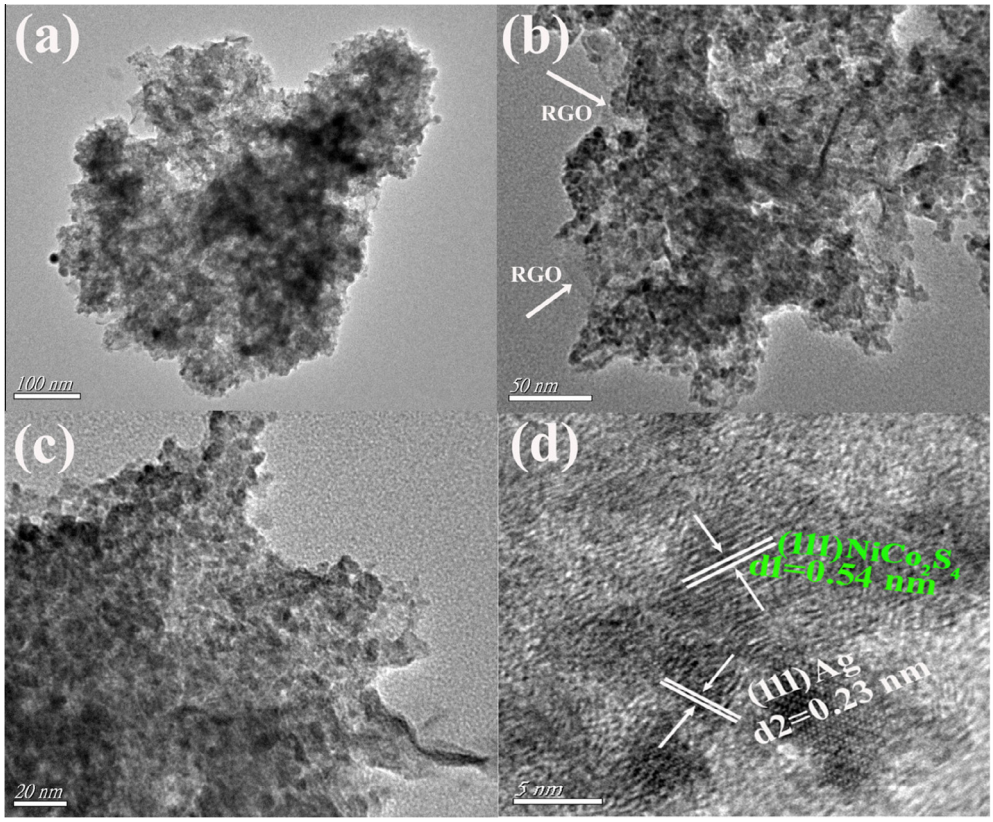

Fig. 3. TEM and HRTEM images of RGO/Ag/$NiCo_2S_4$-3 nanocomposite.

been deposited on during the self-assembly process. It is known that Ag as a heavy atom has strong scattering factor [39]. Therefore, the nanoparticles with darker contrast can be identified as Ag ones, while the ones with lighter contrast as $NiCo_2S_4$ nanoparticles (Fig. 3b and c). The unique structure of $NiCo_2S_4$ nanoparticles deposited on highly conductive Ag is in favor of the charge transfer and transport, which is necessary for relevant redox reaction and thus promotes capacitance generation. The lattice fringes observed in HRTEM image provide further evidence to distinguish Ag and $NiCo_2S_4$ nanoparticles. From Fig. 3d, the lattice space of 0.54 nm can be assigned to the (1 1 1) plane of $NiCo_2S_4$ nanoparticles, while the lattice distance of 0.23 nm detected in much darker particles can be indexed to the (1 1 1) plane of Ag nanoparticle. HRTEM also reveals that the sizes of $NiCo_2S_4$ and Ag nanoparticles are about 8 nm and 4 nm, respectively. $NiCo_2S_4$ with small particle size has much larger specific surface area, therefore more active sites can contact with the electrolyte, which contributes to a higher specific capacitance. The Brunauer-Emmett-Teller surface areas have been tested by a surface area and porosity analyzer (NDVA-2000e), and the nitrogen adsorption and desorption isotherms of RGO/$NiCo_2S_4$, RGO/Ag/$NiCo_2S_4$-1, RGO/Ag/$NiCo_2S_4$-2, RGO/Ag/$NiCo_2S_4$-3, RGO/Ag/$NiCo_2S_4$-4 are displayed in Fig. S5, which reveal that the specific surface areas are 8.78, 3.23, 1.53, 0.71 and 0.28 m^2/g, respectively. Therefore, the specific surface areas decrease with the increasing Ag contents, which can mainly be attributed to the relatively low content of RGO in the nanocomposites. For comparison, the TEM images of RGO/Ag/$NiCo_2S_4$-1, RGO/Ag/$NiCo_2S_4$-2, RGO/Ag/$NiCo_2S_4$-4 and RGO/$NiCo_2S_4$ are displayed in the Fig. S2. It can be observed that $NiCo_2S_4$ nanoparticles tightly attach on RGO/Ag sheets (RGO sheets), well consistent with the case observed in the RGO/Ag/$NiCo_2S_4$-3 nanocomposite.

3.3. Electrochemical properties of RGO/Ag/$NiCo_2S_4$ nanocomposites

To evaluate the electrochemical contribution from Ag, CV and GCD measurements of RGO/$NiCo_2S_4$ and RGO/Ag/$NiCo_2S_4$ nanocomposites electrodes were carried out in a three-electrode system. Fig. 4a shows the CV curves measured at the scan rate of 5 mV s^{-1} with a potential window of 0–0.5 V (vs. SCE). Clearly, all of the CV curves show two oxidation peaks and an integrated reduction peak, which reveal the typical pseudocapacitive characteristic of RGO/$NiCo_2S_4$ and RGO/Ag/$NiCo_2S_4$ nanocomposites. The oxidation peak at around 300 mV is attributed to the oxidation reaction related to Ni^{2+}/Ni^{3+} and Co^{2+}/Co^{3+} [13], while the peak at 380 mV is the oxidation peak of the Ag nanoparticles in KOH solution [40]. Only one integrated reduction peak occurs in the RGO/Ag/$NiCo_2S_4$ spectra, which is attributed to the fact that the reduction peak position of Ag/Ag^+ is close to that of Ni^{2+}/Ni^{3+} and Co^{2+}/Co^{3+}. The specific capacitances from CV curves are calculated by the formula: $C_s = (\int IdV)/(vm\Delta V)$, where I is the response current, ΔV is the potential difference, v is the potential scan rate, and m is the mass of the active materials in the electrodes [41]. Clearly, the specific capacitance is proportional to the integral area of CV curves at the same scan rate [25,42]. The specific capacitances of RGO/Ag/$NiCo_2S_4$-1, RGO/Ag/$NiCo_2S_4$-2, RGO/Ag/$NiCo_2S_4$-3, RGO/Ag/$NiCo_2S_4$-4 and RGO/$NiCo_2S_4$ electrodes at a scan rate of 5 mV s^{-1} are ca. 1143.2 F g^{-1}, 1376.4 F g^{-1}, 1609.2 F g^{-1}, 1161.4 F g^{-1} and 917.4 F g^{-1}, respectively. The improved specific capacitance of the RGO/Ag/$NiCo_2S_4$ nanocomposites can be attributed to the excellent conductivity of Ag nanoparticles [27,43]. Moreover, it can be observed that the encircled area of RGO/Ag/$NiCo_2S_4$ nanocomposites decreases in the order of RGO/Ag/$NiCo_2S_4$-3 > RGO/Ag/$NiCo_2S_4$-2 > RGO/Ag/$NiCo_2S_4$-4 > RGO/Ag/$NiCo_2S_4$-1, which demonstrates that the specific capacitances are affected by the Ag contents. With the increase of

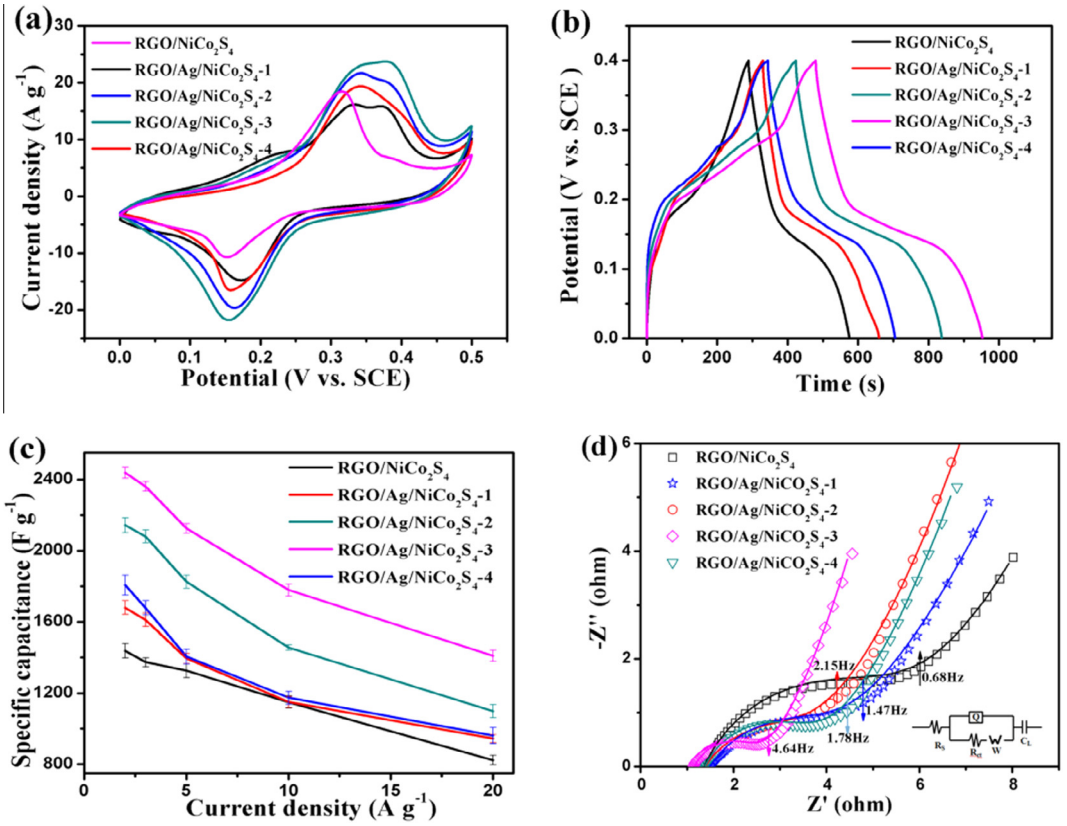

Fig. 4. (a) CV curves of RGO/$NiCo_2S_4$ and RGO/Ag/$NiCo_2S_4$ nanocomposites measured at a scan rate of 5 mV s^{-1}; (b) GCD curves of RGO/$NiCo_2S_4$ and RGO/Ag/$NiCo_2S_4$ nanocomposites tested at the current density of 2 A g^{-1}; (c) the specific capacitance values of RGO/$NiCo_2S_4$ and RGO/Ag/$NiCo_2S_4$ nanocomposites as a function of current density; (d) Nyquist curves of RGO/$NiCo_2S_4$ and RGO/Ag/$NiCo_2S_4$ nanocomposites.

Ag content, the enhanced specific capacitance can be attributed to the improved conductivity of RGO/Ag/$NiCo_2S_4$ nanocomposites. However, too high content of Ag will accordingly reduce the content of the active component ($NiCo_2S_4$), resulting in a decrease in specific capacitances. Therefore, RGO/Ag/$NiCo_2S_4$-3 nanocomposite owns the optimum electrochemical performance. CV curves of RGO/Ag/$NiCo_2S_4$-3 nanocomposite at different scan rates ranging from 5 to 40 mV s^{-1} are displayed in Fig. S3a. With the increasing scan rate, the potentials of the oxidation and reduction peaks shift to a more positive and negative direction, respectively. This happens because the kinetics of the oxidation and reduction reactions is relatively slow and thus the equilibrium is not established rapidly in comparison to the high scan rate, suggesting that the reaction is a quasi-reversible electron transfer reaction. In this situation, the voltage applied will not result in the generation of the concentrations at the electrode surface predicted by Nernst equation, and the current takes more time to respond to the applied voltage than the reversible case. In addition, the height of peak current density increases gradually, suggesting that the product is beneficial for fast redox reaction.

GCD curves of RGO/$NiCo_2S_4$ and RGO/Ag/$NiCo_2S_4$ nanocomposites at the current density of 2.0 A g^{-1} are displayed in Fig. 4b. The discharge voltage plateaus at around 0.15 V can be seen clearly, which match well with the reduction peak potentials in the CV curves. Different from the EDLCs characterized by nearly linear GCD curves, the distinct voltage plateaus demonstrate the faradaic behaviors caused by charge transfer reactions [44]. The GCD curves of RGO/Ag/$NiCo_2S_4$-3 nanocomposite at various current densities ranging from 2.0 to 20 A g^{-1} are presented in Fig. S3b. The average specific capacitance calculated from the discharge curve is according to the following equation:

$$C_s = I\Delta t/(m\Delta V) \quad (1)$$

where C_s (F g^{-1}) is the specific capacitance, I (mA) is the discharge current, Δt (s) represents the discharge time, ΔV (V) is the potential window during discharge, and m (mg) is the mass of the active material (RGO/$NiCo_2S_4$ and RGO/Ag/$NiCo_2S_4$ nanocomposites) within the electrode [44]. The calculated specific capacitances as a function of current density are presented in Fig. 4c. Encouragingly, RGO/Ag/$NiCo_2S_4$-3 nanocomposite has the highest C_s with a maximum value of 2438.3 F g^{-1} at the current density of 2.0 A g^{-1}. Even at a relatively high current density of 20 A g^{-1}, a C_s value of 1410.0 F g^{-1} can be still remained. The above results suggest that RGO/Ag/$NiCo_2S_4$-3 nanocomposite has superior electrochemical capacitance and good rate capability. For comparison, the specific capacitance of RGO/$NiCo_2S_4$ is also calculated. It is found that the specific capacitance of RGO/$NiCo_2S_4$ is much lower than those of the RGO/Ag/$NiCo_2S_4$ nanocomposites under the same current density. Nevertheless, compared with the reported pure $NiCo_2S_4$ [13–16], RGO/$NiCo_2S_4$ in our work still has a relatively higher specific capacitance (1437.5 F g^{-1}) due to the synergistic effect between $NiCo_2S_4$ nanoparticles and RGO. In addition, RGO/$NiCo_2S_4$ and RGO/Ag/$NiCo_2S_4$ nanocomposites display a decrease of C_s with the increase of current density ranging from 2.0 to 20 A g^{-1}. The fading specific capacitances can be ascribed to the limited diffusion rate of OH^- ions. At a lower current density, the OH^- ions have enough time to diffuse into inner of the electrode materials, more active components can be contacted with the electrolyte for capacitance generation. With the increase of current density, the diffusion rate of OH^- anion becomes relatively slow, and thus only the outer active surface of the electrode material can be utilized during the redox process, resulting in a drop in specific capacitance [42].

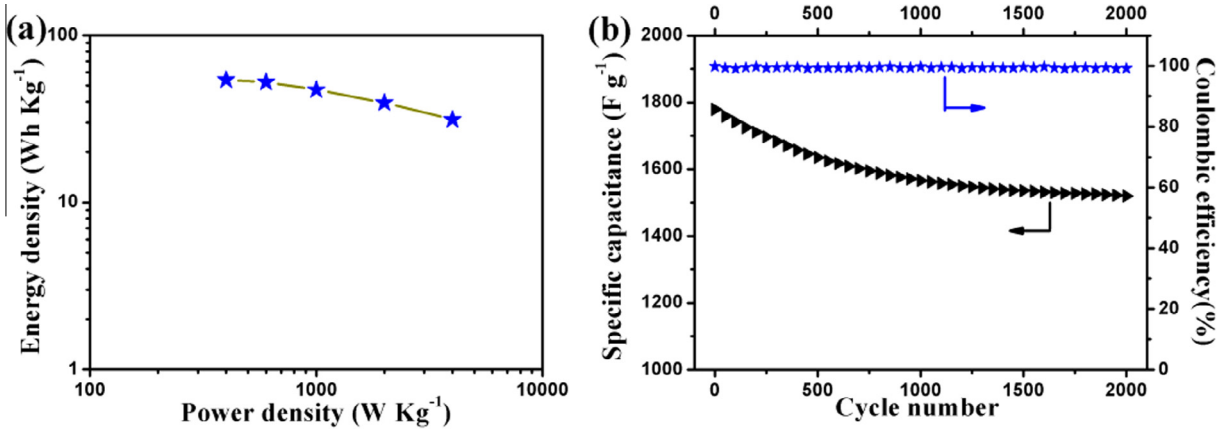

Fig. 5. (a) Ragone plot of the RGO/Ag/$NiCo_2S_4$-3 nanocomposite electrode; (b) cycle performance and Coulombic efficiency for RGO/Ag/$NiCo_2S_4$-3 nanocomposite at a current density of 10 A g^{-1}.

Table 2
Comparison of the specific capacitance between RGO/NiCoS materials and RGO/Ag/$NiCo_2S_4$.

Material	Specific capacitance (F g^{-1})	Current density (A g^{-1})	Electrolyte	Refs
$NiCo_2S_4$	437	1	3 KOH	[13]
$CoNi_2S_4$	1169	1	3 KOH	[42]
$NiCo_2S_4$/NCF	1231	2	6 KOH	[12]
$NiCo_2S_4$/RGO	1451	3	2 KOH	[45]
$CoNi_2S_4$/RGO	2099	1	3 KOH	[25]
RGO/Ag/$NiCo_2S_4$	2438	2	3 KOH	Our work

Electrochemical impedance spectroscopy (EIS) analysis is a principal method for examining the fundamental behavior of electrode materials. EIS was carried out at open circuit potential with an amplitude of 5 mV in the frequency range of 0.1 Hz to 100 kHz. The Nyquist plots of the supercapacitor electrodes based on RGO/$NiCo_2S_4$ and RGO/Ag/$NiCo_2S_4$ nanocomposites are shown in Fig. 4d. An equivalent circuit used to fit the impedance curve is presented in the inset of Fig. 4d, where R_s represents the resistance related to the ionic conductivity of the electrolyte and electronic conductivity of the electrodes and current collectors; Q is the constant phase element accounting for a double-layer capacitance; R_{ct} is the charge-transfer resistance associated with the Faradic reactions; W is the Warburg resistance arising from the ion diffusion and transport in the electrolyte, and C_L is the limit capacitance [45,46]. Electrochemical parameter values are extracted from ZSimpWin programme to fit the equivalent circuit model of R(Q(RW))(C), and the calculated values have been listed in Table S1. It is known that the charge-discharge resistance R_{ct} is a limiting factor for specific power of a supercapacitor. Based on the EIS data, the fitting R_{ct} value for RGO/Ag/$NiCo_2S_4$-3 composite is 1.418 Ω, much lower than those for RGO/Ag/$NiCo_2S_4$-1 (3.046 Ω), RGO/Ag/$NiCo_2S_4$-2 (2.545 Ω), RGO/Ag/$NiCo_2S_4$-4 (2.575 Ω) and RGO/$NiCo_2S_4$ (4.517 Ω), indicating that RGO/Ag/$NiCo_2S_4$-3 has the lowest Faraday resistance. Although the RGO/Ag/$NiCo_2S_4$-4 has the highest Ag content, the excess Ag could result in the agglomeration of Ag nanoparticles in the surface of RGO, which not only decreases the specific surface area, but also makes some Ag nanoparticles inoperative in the electrochemical reaction. The electrochemical reaction of RGO/Ag/$NiCo_2S_4$-4 composite occurred at the interface of electrolyte and electrode is not easier than that of RGO/Ag/$NiCo_2S_4$-3. In addition, the Bode plots of RGO/$NiCo_2S_4$ and RGO/Ag/$NiCo_2S_4$ nanocomposites are shown in Fig. S4. From Fig. S4a, RGO/Ag/$NiCo_2S_4$-3 nanocomposite shows relatively lower |Z| value at the low frequency, suggesting its higher conductivity. It is known that in the low frequency, the phase angle of 90° means ideal capacitive behavior, on the contrary, the phase angle of 0° means pure resistance behavior. From Fig. S4b, it can been observed that the phase angles at the lowest frequency for RGO/$NiCo_2S_4$, RGO/Ag/$NiCo_2S_4$-1, RGO/Ag/$NiCo_2S_4$-2, RGO/Ag/$NiCo_2S_4$-3, RGO/Ag/$NiCo_2S_4$-4 are about 25°, 35°, 45°, 41° and 37°, respectively, suggesting their pseudocapacitive behavior [47,48].

Specific energy (E) and specific power (P) are two key factors for evaluating the power application of supercapacitors. The energy density and power density values are calculated according to GCD curves, and the equations are displayed as follows:

$$E = (C\Delta V^2)/2, P = (Q\Delta V)/(2t) = E/t \quad (2)$$

where E (W h kg^{-1}) is the average energy density, C (F g^{-1}) is specific capacitance, ΔV (V) is the potential window during discharge, P (W kg^{-1}) is the average power density, Q (C) is total charge delivered, and t (s) represents the discharge time. As shown in Fig. 5a, a small energy density decrease can be observed when current density increases from 2 to 20 A g^{-1}. Specifically, the RGO/Ag/$NiCo_2S_4$-3 nanocomposite electrode exhibits a high energy density of 54.2 W h kg^{-1} at a power density of 400.0 W kg^{-1}, and still remains 31.3 W h kg^{-1} at a higher power density of 3999.6 W kg^{-1}. Obviously, RGO/Ag/$NiCo_2S_4$-3 nanocomposite exhibits much higher specific capacitance and energy density as compared with other nickel cobalt sulfide nanomaterials or RGO/nickel cobalt sulfide nanocomposites [12,13,25,44,49]. The results are shown in Table 2. In order to investigate the cycling stability of the RGO/Ag/$NiCo_2S_4$ nanocomposite electrode, the repeated charge/discharge measurement at a constant current density of 10 A g^{-1} was carried out, as shown in Fig. 5b. The specific capacitance gradually decreases with the increase of the cycle number. After 1000 cycles, it turns relatively stable, and 85.4% of the specific capacitance can still be retained at the 2000th cycle. In addition, the charge/discharge efficiency (η), also called Coulombic efficiency, is an important parameter to evaluate the reversibility of the electrode. The equation is applied as follows: $\eta = t_d/t_c \times 100\%$, where t_c and t_d are the charge and discharge times, respectively [25]. The RGO/Ag/$NiCo_2S_4$-3

nanocomposite electrode shows a high electrochemical reversibility with Coulombic efficiency of more than 99% during the entire cycling test. The remarkable supercapacitive performance of RGO/Ag/$NiCo_2S_4$ ternary nanocomposites could be attributed to the following structural features. Firstly, Ag nanoparticles act as the spacer to prevent the adjacent graphene sheets from aggregation, and then RGO/Ag can work as an ideal substrate for anchoring $NiCo_2S_4$ nanoparticles uniformly, thus more electrochemical active components can be contacted with electrolyte for capacitance generation. Secondly, high conductivity of Ag nanoparticles can create the conductive pathways, and thus the incorporation Ag in RGO/$NiCo_2S_4$ nanocomposite can effectively improve the conductivity and facilitate the electron transport and ion diffusion during the charge-discharge process.

4. Conclusions

In conclusion, RGO/Ag/$NiCo_2S_4$ ternary nanocomposites with Ag and $NiCo_2S_4$ nanoparticles homogeneously anchored on the surface of RGO sheets have been successfully prepared. The efficient synthesis involves the in-suit growth of Ag nanoparticles on RGO sheets and subsequent self-assembly of $NiCo_2S_4$ nanoparticles on RGO/Ag nanocomposite. The ternary nanocomposites show a characteristic Faradic capacitance behavior with excellent specific capacitances, good rate capability and high cycling stability. The greatly improved electrochemical performance can be mainly attributed to the introduction of high conductive Ag nanoparticles. They not only act as the spacer to prevent the adjacent graphene sheets from aggregation but also provide efficient conductive pathways for electron transport and ion diffusion. In addition, high redox activity of Ag nanoparticles is in favor of capacitance generation. The remarkable capacitive performance of RGO/Ag/$NiCo_2S_4$ nanocomposites promises prospective application in supercapacitors.

Acknowledgements

The authors are grateful for financial support from Specialized Research Fund for the Doctoral Program of Higher Education of China (No. 20123227110018) and National Nature Science Foundation of China (No. 51272094 and 51303204).

Appendix A. Supplementary data

Supplementary data associated with this article can be found, in the online version, at http://dx.doi.org/10.1016/j.cej.2016.09.059.

References

[1] H.B. Wu, H. Pang, X.W. Lou, Facile synthesis of mesoporous $Ni_{0.3}Co_{2.7}O_4$ hierarchical structures for high-performance supercapacitors, Energy Environ. Sci. 6 (2013) 3619–3626.
[2] J.H. Zhao, J.Z. He, M.J. Sun, M.J. Qu, H. Pang, Nickel hydroxide–nickel nanohybrids indirectly from coordination microfibers for high performance supercapacitor electrodes, Inorg. Chem. Front. 2 (2015) 129–135.
[3] B. Li, M.B. Zheng, H.G. Xue, H. Pang, High performance electrochemical capacitor materials focusing on nickel based materials, Inorg. Chem. Front. 3 (2016) 175–202.
[4] J. Xu, Q.F. Wang, X.W. Wang, Q.Y. Xiang, B. Hang, D. Chen, G.Z. Shen, Flexible asymmetric supercapacitors based upon Co_9S_8 nanorod//Co_3O_4@RuO_2 nanosheet arrays on carbon cloth, ACS Nano 7 (2013) 5453–5462.
[5] X.F. Wang, B. Liu, R. Liu, Q.F. Wang, X.J. Hou, D. Chen, R.M. Wang, G.Z. Shen, Fiber-based flexible all-solid-state asymmetric supercapacitors for integrated photodetecting system, Angew. Chem. Int. Ed. 53 (2014) 1849–1853.
[6] H. Chen, L.F. Hu, M. Chen, Y. Yan, L.M. Wu, Nickel–cobalt layered double hydroxide nanosheets for high-performance supercapacitor electrode materials, Adv. Funct. Mater. 24 (2014) 934–942.
[7] G.L. Li, C.L. Xu, Hydrothermal synthesis of 3D $Ni_xCo_{1-x}S_2$ particles/graphene composite hydrogels for high performance supercapacitors, Carbon 90 (2015) 44–52.
[8] Z.H. Wen, X.C. Wang, S. Mao, Z. Bo, H. Kim, S.M. Cui, G.H. Lu, X.L. Feng, J.H. Chen, Crumpled nitrogen-doped graphene nanosheets with ultrahigh pore volume for high performance supercapacitor, Adv. Mater. 41 (2012) 5610–5616.
[9] X.H. Xia, C.R. Zhu, J.S. Luo, Z.Y. Zeng, C. Guan, C.F. Ng, H. Zhang, H.J. Fan, Synthesis of free-standing metal sulfide nanoarrays via anion exchange reaction and their electrochemical energy storage application, Small 10 (2014) 766–773.
[10] S.J. Peng, L.L. Li, H.T. Tan, R. Cai, W.H. Shi, C.C. Li, S.G. Mhaisalkar, M. Srinivasan, S. Ramakrishna, Q.Y. Yan, MS_2 (M = Co and Ni) hollow spheres with tunable interiors for high-performance supercapacitors and photovoltaics, Adv. Funct. Mater. 24 (2014) 2155–2162.
[11] Q.H. Wang, L.F. Jiao, H.M. Du, Y.C. Si, Y.J. Wang, H.T. Yuan, Co_3S_4 hollow nanospheres grown on graphene as advanced electrode materials for supercapacitors, J. Mater. Chem. 22 (2012) 21387–21391.
[12] L.F. Shen, J. Wang, G.Y. Xu, H.S. Li, H. Dou, X.G. Zhang, $NiCo_2S_4$ nanosheets grown on nitrogen-doped carbon foams as an advanced electrode for supercapacitors, Adv. Energy Mater. 5 (2014) 1400977.
[13] J. Pu, F.L. Cui, S.B. Chu, T.T. Wang, E.H. Sheng, Z.H. Wang, Preparation and electrochemical characterization of hollow hexagonal $NiCo_2S_4$ nanoplates as pseudocapacitor materials, ACS Sustain. Chem. Eng. 2 (2014) 809–815.
[14] Y.F. Zhang, M.Z. Ma, J. Yang, C.C. Sun, H.Q. Su, W. Huang, X.C. Dong, Shape-controlled synthesis of $NiCo_2S_4$ and their charge storage characteristics in supercapacitors, Nanoscale 6 (2014) 9824–9830.
[15] L. Yu, L. Zhang, H.B. Wu, X.W. (David) Lou, Formation of $Ni_xCo_{3-x}S_4$ hollow nanoprisms with enhanced pseudocapacitive properties, Angew. Chem. Int. Ed. 53 (2014) 3711–3714.
[16] J. Pu, T.T. Wang, H.Y. Wang, Y. Tong, C.C. Lu, W. Kong, Z.H. Wang, Direct growth of $NiCo_2S_4$ nanotube arrays on nickel foam as high-performance binder-free electrodes for supercapacitors, ChemPlusChem 79 (2014) 577–583.
[17] H.C. Chen, J.J. Jiang, L. Zhang, D.D. Xia, Y.D. Zhao, D.Q. Guo, T. Qi, H.Z. Wan, In situ growth of $NiCo_2S_4$ nanotube arrays on Ni foam for supercapacitors: Maximizing utilization efficiency at high mass loading to achieve ultrahigh areal pseudocapacitance, J. Power Sources 254 (2014) 249–257.
[18] H.Z. Wan, J.J. Jiang, J.W. Yu, K. Xu, L. Miao, L. Zhang, H.C. Chen, Y.J. Ruan, $NiCo_2S_4$ porous nanotubes synthesis via sacrificial templates: high-performance electrode materials of supercapacitors, CrystEngComm 15 (2013) 7649–7651.
[19] M.J. Zhi, C.C. Xiang, J.T. Li, M. Li, N.Q. Wu, Nanostructured carbon–metal oxide composite electrodes for supercapacitors: a review, Nanoscale 5 (2013) 72–88.
[20] J. Memon, J.H. Sun, D.L. Meng, W.Z. Ouyang, M.A. Memon, Y. Huang, S. Yan, J.X. Geng, Synthesis of graphene/Ni–Al layered double hydroxide nanowires and their application as an electrode material for supercapacitors, J. Mater. Chem. A 2 (2014) 5060–5067.
[21] S. Stankovich, D.A. Dikin, G.H.B. Dommett, K.M. Kohlhaas, E.J. Zimney, E.A. Stach, R.D. Piner, S.T. Nguyen, R.S. Ruoff, Graphene-based composite materials, Nature 442 (2006) 282–286.
[22] A.K. Geim, Graphene: status and prospects, Science 324 (2009) 1530–1534.
[23] Y.J. Chen, J. Zhu, B.H. Qu, B.A. Lu, Z. Xu, Graphene improving lithium-ion battery performance by construction of $NiCo_2O_4$/graphene hybrid nanosheet arrays, Nano Energy 3 (2014) 88–94.
[24] L. Wang, X.H. Wang, X.P. Xiao, F.G. Xu, Y.J. Sun, Z. Li, Reduced graphene oxide/nickel cobaltite nanoflake composites for high specific capacitance supercapacitors, Electrochim. Acta 111 (2013) 937–945.
[25] W.M. Du, Z.Y. Wang, Z.Q. Zhu, S. Hu, X.Y. Zhu, Y.F. Shi, H. Pang, X.F. Qian, Facile synthesis and superior electrochemical performances of $CoNi_2S_4$/graphene nanocomposite suitable for supercapacitor electrodes, J. Mater. Chem. A 2 (2014) 9613–9619.
[26] L.B. Ma, X.P. Shen, Z.Y. Ji, G.X. Zhu, H. Zhou, Ag nanoparticles decorated MnO_2/reduced graphene oxide as advanced electrode materials for supercapacitors, Chem. Eng. J. 252 (2014) 95–103.
[27] R. Pasricha, A. Gupta, A.K. Srivastava, A facile and novel synthesis of Ag–graphene-based nanocomposites, Small 5 (2009) 2253–2259.
[28] W.S. Hummers, R.E. Offeman, Preparation of graphitic oxide, J. Am. Chem. Soc. 80 (1958), 1339-1339.
[29] L.B. Ma, X.P. Shen, Z.Y. Ji, S. Wang, H. Zhou, G.X. Zhu, Carbon coated nickel sulfide/reduced graphene oxide nanocomposites: facile synthesis and excellent supercapacitor performance, Electrochim. Acta 146 (2014) 525–532.
[30] X.B. Fan, W.C. Peng, Y. Li, X.Y. Li, S.L. Wang, G.L. Zhang, F.B. Zhang, Deoxygenation of exfoliated graphite oxide under alkaline conditions: a green route to graphene preparation, Adv. Mater. 20 (2008) 4490–4493.
[31] P. Wang, L. Han, C.Z. Zhu, Y.M. Zhai, S.J. Dong, Aqueous-phase synthesis of Ag–TiO_2–reduced graphene oxide and Pt–TiO_2–reduced graphene oxide hybrid nanostructures and their catalytic properties, Nano Res. 4 (2011) 1153–1162.
[32] A.C. Ferrari, J.C. Meyer, V. Scardaci, C. Casiraghi, M. Lazzeri, F. Mauri, Raman spectrum of graphene and graphene layers, Phys. Rev. Lett. 97 (2006), 187401.
[33] F. Tuinstra, J.L. Koenig, Raman spectrum of graphite, J. Chem. Phys. 53 (1970) 1126–1130.
[34] M.S. Dresselhaus, A. Jorio, M. Hofmann, G. Dresselhaus, R. Saito, Perspectives on carbon nanotubes and graphene Raman spectroscopy, Nano Lett. 10 (2010) 751–758.
[35] M.M. Lucchese, F. Satavle, E.H.M. Ferreira, C. Vilani, M.V.O. Moutinho, R.B. Capaz, C.A. Achete, A. Jorio, Quantifying ion-induced defects and Raman relaxation length in graphene, Carbon 48 (2010) 1592–1597.
[36] C. Xu, X. Wang, J.W. Zhu, Graphene–Metal Particle Nanocomposites, J. Phys. Chem. C 112 (2008) 19841–19845.

[37] W.F. Chen, L.F. Yan, P.R. Bangal, Chemical reduction of graphene oxide to graphene by sulfur-containing compounds, J. Phys. Chem. C 114 (2010) 19885–19890.
[38] J. Yang, M.Z. Ma, C.C. Sun, Y.F. Zhang, W. Huang, X.C. Dong, Hybrid $NiCo_2S_4$@MnO_2 heterostructures for high performance supercapacitor electrodes, J. Mater. Chem. A 3 (2015) 1258–1264.
[39] T. Akita, M. Kohyama, M. Haruta, Electron microscopy study of gold nanoparticles deposited on transition metal oxides, Acc. Chem. Res. 46 (2013) 1773–1782.
[40] A. Bello, M. Fabiane, D. Dodoo-Arhin, K.I. Ozoemena, N. Manyala, Silver nanoparticles decorated on a three-dimensional graphene scaffold for electrochemical applications, J. Phys. Chem. Solids 75 (2014) 109–114.
[41] J.C. Chen, C.T. Hsu, C.C. Hu, Superior capacitive performances of binary nickel–cobalt hydroxide nanonetwork prepared by cathodic deposition, J. Power Sources 253 (2014) 205–213.
[42] L. Mei, T. Yang, C. Xu, M. Zhang, L.B. Chen, Q.H. Li, T.H. Wang, Hierarchical mushroom-like $CoNi_2S_4$ arrays as a novel electrode material for supercapacitors, Nano Energy 3 (2014) 36–45.
[43] G.N. Zhang, L. Zheng, M. Zhang, S.H. Guo, Z.H. Liu, Z.P. Yang, Z.L. Wang, Preparation of Ag-nanoparticle-loaded MnO_2 nanosheets and their capacitance behavior, Energy Fuels 26 (2012) 618–623.
[44] W.M. Du, Z.Q. Zhu, Y.B. Wang, J.N. Liu, W.J. Yang, X.F. Qian, H. Pang, One-step synthesis of $CoNi_2S_4$ nanoparticles for supercapacitor electrodes, RSC Adv. 4 (2014) 6998–7002.
[45] Y.H. Li, L.J. Cao, L. Qiao, M. Zhou, Y. Yang, P. Xiao, Y.H. Zhang, Ni–Co sulfide nanowires on nickel foam with ultrahigh capacitance for asymmetric supercapacitors, J. Mater. Chem. A 2 (2014) 6540–6548.
[46] X. Wang, W.S. Liu, X.H. Lu, P.S. Lee, Dodecyl sulfate-induced fast faradic process in nickel cobalt oxide–reduced graphite oxide hybrid material and its application for asymmetric supercapacitor device, J. Mater. Chem. 22 (2012) 23114–23119.
[47] L. Yuan, X.H. Lu, X. Xiao, T. Zhai, J. Dai, F. Zhang, F.C. Zhang, B. Hu, X. Wang, L. Gong, J. Chen, Flexible solid-state supercapacitors based on carbon nanoparticles/MnO_2 nanorods hybrid structure, ACS Nano 6 (2012) 656–661.
[48] K. Krishnamoorthy, G.K. Veerasubramani, S. Radhakrishnan, S.J. Kim, One pot hydrothermal growth of hierarchical nanostructured Ni_3S_2 on Ni foam for supercapacitor application, Chem. Eng. J. 251 (2014) 116–122.
[49] S.J. Peng, L.L. Li, C.C. Li, H.T. Tan, R. Cai, H. Yu, S. Mhaisalkar, M. Srinivasan, S. Ramakrishna, Q.Y. Yan, In situ growth of $NiCo_2S_4$ nanosheets on graphene for high-performance supercapacitors, Chem. Commun. 49 (2013) 10178–10180.